ChemPubSoc Europe

DOI: 10.1002/celc.201700425

CHEMELECTROCHEM Articles

Ethanol Oxidation Reaction Catalyzed by Palladium Nanoparticles Supported on Hydrogen-Treated TiO_2 Nanobelts: Impact of Oxygen Vacancies

Bingzhang Lu[+,a] Bin Yao[+,a] Graham Roseman,[a] Christopher P. Deming,[a] Jia En Lu,[a] Glenn L. Millhauser,[a] Yat Li,[a] and Shaowei Chen*[a]

Nanocomposites based on palladium nanoparticles deposited onto TiO_2 nanobelts were prepared by chemical reduction of Pd (II) precursors and the catalytic activity towards ethanol oxidation reaction (EOR) was examined and compared within the context of TiO_2 oxygen vacancies formed by thermal annealing at controlled temperatures (400–600 °C) in a hydrogen atmosphere. Transmission electron microscopic measurements showed that the Pd nanoparticles (about 5 nm in diameter) were clustered somewhat on the surfaces of hydrogen-treated TiO_2 nanobelts ($Pd/hTiO_2$), but distributed rather evenly on the untreated ones (Pd/TiO_2). X-ray photoelectron spectroscopic studies suggested electron transfer from Ti to Pd in the $Pd/hTiO_2$ samples, as compared to untreated Pd/TiO_2, due to the formation of oxygen vacancies in TiO_2 nanobelts where the concentration increased with increasing thermal annealing temperature, as evidenced in electron paramagnetic resonance measurements. Significantly, electrochemical measurements showed markedly enhanced EOR activity of both Pd/TiO_2 and $Pd/hTiO_2$ in alkaline media, as compared to commercial Pd/C, and the activity increased drastically with the concentration of oxygen vacancies, most likely because oxygen vacancies facilitated the formation of hydroxyl species on the TiO_2 surface that played a critical role in the oxidation of ethanol to acetate.

1. Introduction

Direct ethanol fuel cells (DEFCs) represent a unique fuel cell technology that has been attracting extensive interest,[1] largely because of the remarkable energy density of ethanol (8.01 KWh/Kg), ready availability of ethanol by fermentation, low toxicity, and ease of storage and transportation, as compared to other fuels such as hydrogen, methanol and formic acid.[2] In addition, ethanol has a large molecule weight that can minimize the "crossover" effect.[3] While both acidic and alkaline electrolytes have been used in DEFCs, the electron-transfer kinetics of both ethanol oxidation at the anode and oxygen reduction at the cathode has been found to be faster in alkaline media than in acidic media.[4] In general, there are two major pathways of ethanol oxidation in alkaline media. One involves 12-electron, complete oxidation of ethanol to CO_3^{2-}, and the other is a 4-electron process, where ethanol is oxidized into acetaldehyde and acetate only.[5] Certainly, to maximize fuel cell efficiency, the former pathway is desired; however, it is challenging to break the C–C bonds. Thus, developing catalysts for effective oxidation of ethanol has remained an important research topic of alkaline DEFCs. Currently, platinum-based nanoparticles have been the catalysts of choice for DEFC reactions.[6] Yet, because of high costs and limited reserves, the practical applications of Pt-based catalysts have been markedly hampered; in addition, platinum-based catalysts are known to be prone to CO poisoning.[7]

Within such a context, palladium-based nanoparticles have been used as an effective alternative for the electrocatalytic oxidation of ethanol, largely because of its apparent EOR activity and tolerance against CO poisoning.[8] Two strategies are generally employed to improve the use of the catalysts (and thus to reduce the costs) and to enhance the activity. One is to prepare binary or ternary alloys, where the activities may be enhanced by the electronic effects and/or geometrical strains. For example, Jeon et al. prepared a series of graphene-supported Pd_xNi_{100-x} alloy nanoparticles and found that the $Pd_{50}Ni_{50}$ sample exhibited the best activity among the series toward ethanol oxidation, with acetic acid being the primary product.[9] Jiang et al. used P dopants to successfully increase EOR performance of PdNi alloys and observed that acetate was the final product.[10] In another study,[11] Li and coworkers grew PdCo nanotubes on carbon fiber cloth, and the resulting nanocomposites exhibited enhanced EOR activity and resistance against CO poisoning, as compared to the monometallic Pd counterparts. The other strategy involves the use of highly conductive materials, such as N-doped carbon,[12] molybdenum carbide,[13] tungsten carbide,[14] and titanium nitride,[15] as catalyst supports, which may exert synergistic effects on the electronic structure of the metal catalysts as well as enhance the durability of the catalysts. In addition, transition-metal oxides have also been used as catalyst supports,[16] primarily because of their low costs, high natural abundance, low toxicity and high durability in alkaline media.[17] Among these, in

[a] B. Lu,[+] B. Yao,[+] G. Roseman, Dr. C. P. Deming, J. E. Lu, Prof. Dr. G. L. Millhauser, Prof. Dr. Y. Li, Prof. Dr. S. Chen
Department of Chemistry and Biochemistry, University of California, 1156 High Street, Santa Cruz, California 95064, USA
E-mail: shaowei@ucsc.edu
[+] These authors contribute equally.

Supporting information for this article is available on the WWW under https://doi.org/10.1002/celc.201700425

contrast to other metal oxides such as Al_2O_3 and SiO_2, TiO_2 is a reducible oxide and can generate oxygen vacancies upon controlled chemical reduction, which may be exploited as a unique variable in the manipulation of the electrocatalytic activity of the metal nanoparticles towards EOR.[18] Note that for ethanol oxidation on palladium catalysts, it is generally accepted that the dissociative adsorption of ethanol onto the catalyst surface is a rapid process, and the rate-determining step is the desorption of the ethoxy moieties (CH_3CO_{ads}) by adsorbed hydroxy groups (OH_{ads}) on the Pd surface, forming acetate as the final product.[10,19] This may be facilitated by using oxygen-deficient TiO_2 as the supporting substrate, where oxygen vacancies are known to be advantageous for the formation of OH_{ads} species.[20] Additional benefits may arise from the strong metal-support interactions that manipulate the bonding interactions between palladium and carbonaceous intermediates.[18a] This is the primary motivation of the present study.

Herein, a facile wet chemistry method was employed to deposit palladium nanoparticles on TiO_2 nanobelts. Oxygen vacancies in TiO_2 were produced by thermal treatment at elevated temperatures in a hydrogen atmosphere, and evaluated by electron paramagnetic resonance (EPR) measurements. Electrochemical measurements showed that the resulting nanocomposites exhibited apparent electrocatalytic activity towards ethanol oxidation, which was markedly enhanced with oxygen vacancies, in comparison to commercial Pd/C catalysts.

2. Results and Discussion

In the present study, palladium nanoparticles were deposited onto TiO_2 nanobelts with and without hydrogen treatment, and the resulting nanocomposites were referred to as Pd/hTiO_2-T (with T being the temperature for hydrogen treatment, 400, 500, or 600 °C) and Pd/TiO_2, respectively. Figure 1 depicts the representative TEM images of the (A) Pd/TiO_2 and (B) Pd/hTiO_2-600 nanobelt hybrids, respectively. One can see that the TiO_2 nanobelts exhibited a width of *ca.* 70 nm and length ranging from a few hundred nm up to several microns, along with well-defined lattice fringes (Figure 1C) where the interplanar distance of 0.35 nm was consistent with the d-spacing of the (110) crystalline planes of TiO_2(B).[21] From Figure 1A, one can see that in Pd/TiO_2, a number of palladium nanoparticles of about 5 nm in diameter were rather uniformly distributed on the TiO_2 nanobelt surfaces, with no apparent agglomeration. In contrast, for the Pd/hTiO_2-600 sample in Figure 1B, the Pd nanoparticles could be identified only on a certain section of the TiO_2 nanobelts, forming a bamboo-like structure of the resulting hybrids. This is likely because after hydrogen treatment, the TiO_2 nanobelt surface was (partially) reduced, and the sections with enhanced electron density served as the preferred binding sites for Pd deposition. Furthermore, one can see that the palladium nanoparticles also exhibited well-defined lattice fringes where the interplanar spacing of 0.22 nm is in good agreement with the separation of the (111) crystalline planes of *fcc* Pd (Figure 1C).[16f] Similar behaviors were observed with Pd/hTiO_2-400 and Pd/hTiO_2-500. Notably, X-ray diffraction (XRD) studies (Figure S1) showed that hydrogen treatment at 400–600 °C did not alter the crystalline structure of the TiO_2 nanobelts which belonged to monoclinic TiO_2(B) (JCPDS 74-1940).

The formation of Pd/TiO_2 and Pd/hTiO_2 nanocomposites was also evidenced in XPS measurements. From the survey spectra in Figure 2A, the Pd 3d electrons can be readily identified at ca. 335 eV, Pd 3p electrons at 562 eV, Ti 2p electrons at 458 eV and O 1s electrons at 531 eV (along with C 1s electrons of residual carbon at around 285 eV) for both Pd/TiO_2 and Pd/hTiO_2 hybrids. In high-resolution scans, one can see from panel (B) that the Pd 3d electrons exhibited a doublet at 340.6 and 335.3 eV for Pd/TiO_2, corresponding to a spin-orbit coupling of 5.3 eV, consistent with those of metallic Pd;[22] and the binding energies are about 0.4 eV lower for Pd/hTiO_2 at 340.2 and 334.9 eV. From panel (C), the doublet for Ti $2p_{3/2}$ and $2p_{1/2}$ electrons can be found at 458.8 and 464.5 eV for Pd/TiO_2, with a spin-orbit coupling of 5.7 eV, in good agreement with Ti (IV) in TiO_2;[23] yet in Pd/hTiO_2 the binding energies are somewhat higher at 459.0 and 464.8 eV. This suggests charge transfer from Ti to Pd, likely due to the formation of oxygen vacancies by hydrogen treatment of the TiO_2 nanobelts. For O 1s electrons in panel (D), Pd/TiO_2 exhibited two peaks at the binding energies of 530.1 and 532.6 eV, which may be ascribed to oxygen in TiO_2 and hydroxyl groups adsorbed on the TiO_2 surfaces, respectively.[24] For Pd/hTiO_2, whereas the binding

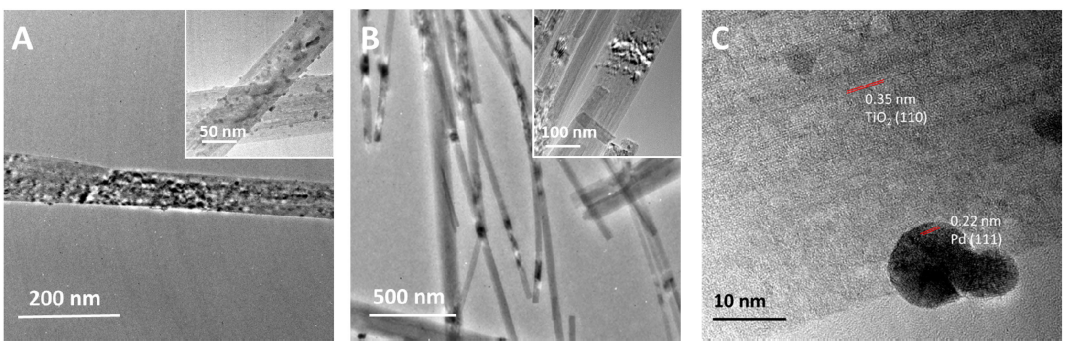

Figure 1. Representative TEM images of A) Pd/TiO_2 and B) Pd/hTiO_2-600. Insets: The corresponding TEM images at higher magnification. Panel (C) is a high-resolution TEM image of Pd/TiO_2 hybrids that depicts the lattice fringes..

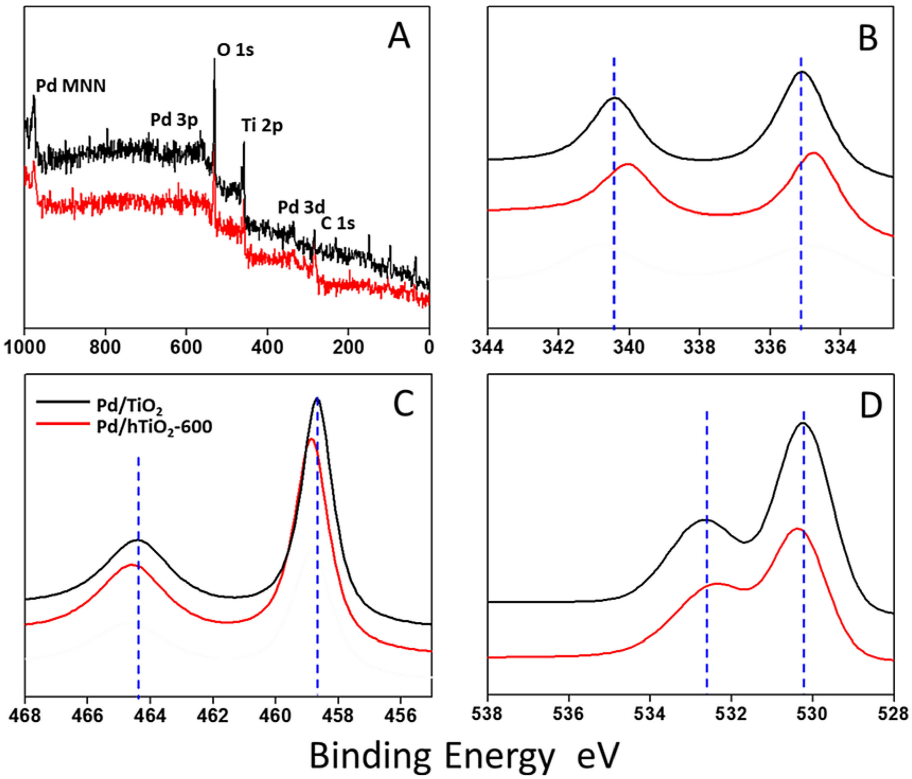

Figure 2. A) XPS survey spectra and high resolution scans of B) Pd 3d, C) Ti 2p and D) O 1s electrons of Pd/TiO_2 and $Pd/hTiO_2$-600 nanocomposites.

energy of surface hydroxyl groups remained invariant at 532.6 eV, the TiO_2 oxygen binding energy is somewhat higher at 530.3 eV, suggesting that the TiO_2 nanobelts indeed became oxygen-deficient after hydrogen treatment.[25] In addition, based on the integrated peak areas, the Pd mass contents in the nanocomposites were found to be rather consistent at 13.3 wt.% for Pd/TiO_2 and 15.1 wt.% for $Pd/hTiO_2$.

EPR studies further supported the notion that oxygen vacancies were formed in the nanocomposites that had been subjected to hydrogen treatment. As shown in Figure 3, one

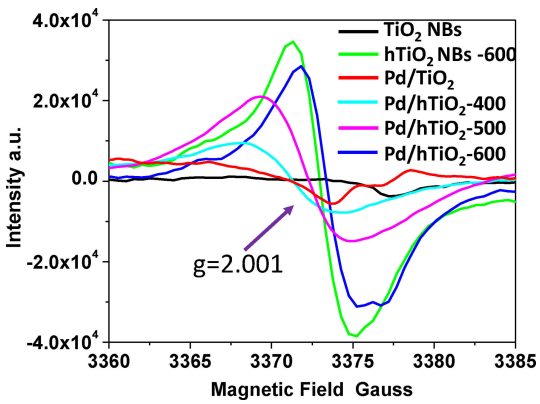

Figure 3. EPR spectra of TiO_2 nanobelts, Pd/TiO_2, and Pd/TiO_2-T nanocomposites.

can see that the as-produced TiO_2 nanobelts (black curve) exhibited only a featureless profile within the magnetic field strength of 3360 to 3385 G, and a similar response was observed after Pd deposition (red curve), suggesting that $NaBH_4$ reduction (for the synthesis of Pd nanoparticle) did not cause marked changes of the TiO_2 structures. Yet, a well-defined resonance emerged at *ca.* 3370 G after hydrogen treatment, and the resonance became increasingly intensified with increasing thermal treatment temperature from 400 to 600 °C (aqua blue, magenta, and blue curves), with the corresponding g value estimated to be 2.001.[26] A similar profile was observed without the deposition of Pd nanoparticle (green curve). This suggests the formation of unpaired electrons being trapped in TiO_2, as a result of partial reduction of TiO_2 by hydrogen treatment,[27] and the concentration of oxygen vacancies increased with increasing thermal annealing temperature, consistent with the results in XPS measurements (Figure 2).

Significantly, the nanocomposites prepared above exhibited apparent electrocatalytic activity towards ethanol oxidation. Figure 4 shows the cyclic voltammograms of the nanocomposites in 1 M KOH with and without 0.1 M ethanol at the potential sweep rate of 50 mV/s, using commercial 20 wt.% Pd/C as the reference. It can be seen that in 1 M KOH alone, all samples exhibited a cathodic peak at +0.634 V, arising from the reduction of palladium oxide formed during the anodic scan. From the integrated peak area,[28] the effective electrochemical surface area (ECSA, Table 1) of the nanocomposite catalysts was estimated to be 5.29 m^2/g_{Pd} for Pd/TiO_2, 14.2 m^2/g_{Pd} for $Pd/hTiO_2$-400, 6.15 m^2/g_{Pd} for $Pd/hTiO_2$-500, and 11.00 m^2/g_{Pd} for

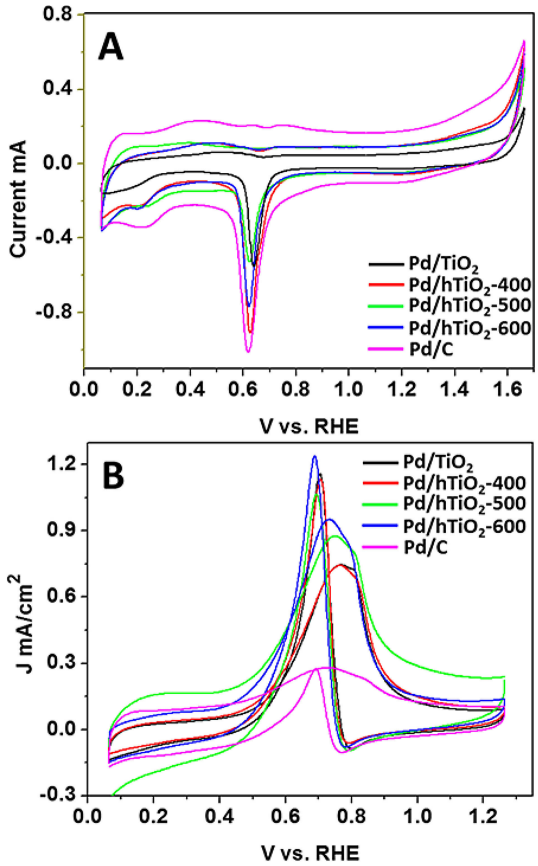

Figure 4. Cyclic voltammograms of a glassy carbon electrode (0.196 cm^2) modified with a calculated amount of Pd/TiO_2, $Pd/hTiO_2$ and Pd/C. The data in panel (A) were acquired in 1 M KOH only, and those in panel (B) were in a solution containing 1 M KOH along with 0.1 M ethanol. The potential scan rate is 50 mV/s. The catalyst loading is 100 μg for Pd/TiO_2 and $Pd/hTiO_2$ nanocomposites, and 50 μg for Pd/C.

Table 1. Summary of the EOR performance of Pd/TiO_2, $Pd/hTiO_2$-600 and Pd/C

Sample	Pd/TiO_2	$Pd/hTiO_2$-600	Pd/C
Pd loading wt% by XPS	13.3	15.1	20
E_{onset} [V vs. RHE]	0.456	0.377	0.469
$E_{p,a}$ [V vs. RHE]	0.769	0.728	0.730
J_a [mA cm^{-2}]	0.68	0.88	0.17
$E_{p,c}$ [V vs. RHE]	0.703	0.687	0.692
J_c [mA cm^{-2}]	1.25	1.31	0.37
J_a/J_c	0.50	0.44	0.40
ECSA [$m^2 g_{Pd}^{-1}$]	5.29	11.00	18.35
R_{ct} [Ω, at +0.7 V]	1557	468	1328

$Pd/hTiO_2$-600, in comparison with 18.35 m^2/g_{Pd} for Pd/C, likely due to the smaller size of the Pd nanoparticles in Pd/C than those in the nanocomposites (Figure 1).

With the addition of 0.1 M ethanol into the electrolyte solution, drastic differences were observed. From Figure 4B, one can see that all samples exhibited a clearly defined oxidation peak in both the anodic and cathodic scans at approximately the same electrode potentials, suggesting apparent electrocatalytic activity towards ethanol oxidation. Yet, a close analysis showed that the performance actually varied among the series of the nanocomposites. For instance, for the Pd/TiO_2 nanocomposites, in the anodic scan, nonzero oxidation currents started to emerge at *ca.* +0.456 V, and reached a maximum at +0.769 V with a peak current density of 0.68 mA/cm^2; in the reverse potential scan, the oxidation peak appeared at +0.703 V with a current density of 1.25 mA/cm^2. Yet when TiO_2 nanobelts were subjected to hydrogen treatment prior to Pd nanoparticle deposition, the resulting nanocomposites exhibited markedly enhanced EOR activity. For instance, the onset potential (E_{onset}), anodic peak potential ($E_{p,a}$), and anodic peak current density (J_a) are +0.396 V, +0.767 V, and 0.65 mA/cm^2 for $Pd/hTiO_2$-400, +0.408 V, +0.748 V, and 0.70 mA/cm^2 for $Pd/hTiO_2$-500, and +0.377 V, +0.728 V and +0.88 mA/cm^2 for $Pd/hTiO_2$-600. Apparently, $Pd/hTiO_2$-600 stood out as the best among the series (Table 1). Remarkably, these nanocomposites all exhibited a drastically better performance than commercial 20 wt.% Pd/C, where the onset potential was identified at +0.464 V, anodic peak at +0.734 V (peak current density 0.17 mA/cm^2), and cathodic peak at +0.694 V (peak current density 0.37 mA/cm^2). These results are summarized in Table 1, from which one can see that the EOR performance increased in the order of Pd/C < Pd/TiO_2 < $Pd/hTiO_2$-400 < $Pd/hTiO_2$-500 < $Pd/hTiO_2$-600. A similar trend was observed with the mass activity, where the anodic mass activity of $Pd/hTiO_2$-600 (59.75 mA/mg_{Pd}) was about twice that of Pd/TiO_2 (33.06 mA/mg_{Pd}) and Pd/C (25.42 mA/mg_{Pd}), as showed in Figure S2.

Mechanistically, the electrochemical oxidation of ethanol is generally believed to involve the following steps [Eqs. (1)–(4)]:[10,19]

$$Pd + CH_3CH_2OH \rightarrow Pd\text{-}(CH_3CH_2OH) \quad (1)$$

$$Pd\text{-}(CH_3CH_2OH) + 3OH^- \rightarrow Pd\text{-}(CH_3CO) + 3H_2O + 3e \quad (2)$$

$$Pd\text{-}(CH_3CO) + Pd\text{-}(OH) \rightarrow Pd\text{-}(CH_3COOH) + Pd \quad (3)$$

$$Pd\text{-}(CH_3COOH) + OH^- \rightarrow Pd + CH_3COO^- + H_2O \quad (4)$$

where adsorption of ethanol molecules on the Pd surfaces is a critical first step (1); the adsorbed ethanol then undergoes three-electron oxidation into ethoxi (2), which reacts further with surface hydroxyl groups to produce acetate (3); and the acetate then desorbs from the electrode surface as the final product (4). In the anodic scan, the reaction kinetics was initially enhanced at increasingly positive electrode potentials, reached a maximum and then decreased with a further increase of the electrode potential because of the formation of palladium oxide (Figure 4A), which passivated the catalyst surface. In the reverse (cathodic) scan, the palladium oxide was electrochemically reduced, leading to the regeneration of a "clean" catalyst surface that exhibited obvious electrocatalytic activity towards ethanol oxidation. Thus, a higher ratio of the anodic to cathodic peak currents (J_a/J_c) suggests the generation of less poisoning intermediates on the Pd surface.[9] From Figure 4B, the ratio was estimated to be 0.50 for Pd/TiO_2 and 0.44 for $Pd/hTiO_2$-600, both higher than that (0.40) of Pd/C (Table 1), suggesting enhanced efficiency in the electrocatalytic oxidation of ethanol

by the Pd/TiO_2 and Pd/hTiO_2 nanocomposites as conpared to commercial Pd/C.

In the present study, the fact that the electrocatalytic activity of Pd/TiO_2 and Pd/hTiO_2 nanocomposites was markedly better than that of Pd/C suggests a synergistic interaction between TiO_2 and Pd nanoparticles in EOR. This can be accounted for by the strong interactions between TiO_2 and Pd, as TiO_2 favored the formation of adsorbed OH species which helped strip absorbed ethoxy intermediates from the Pd surface, and the impacts were enhanced with oxygen-deficient TiO_2, leading to improved activity in ethanol oxidation.[20,29] In the present study, Pd/hTiO_2-600 outperformed others in the series because of its highest concentration of oxygen vacancies (Figure 3).

Significantly, the EOR performance of Pd/hTiO_2-600 was highly comparable to, and in some cases even better than, results reported in recent literature with relevant Pd-based nanocomposites (Table 2). For instance, Cai et al. deposited a Pd monolayer on the surface of *ca.* 10 nm Au nanoparticles, and the catalysts showed an onset and peak potential at +0.44 V and +0.85 V, respectively, in a solution of 1 M KOH and 1 M EtOH, where the peak current was estimated to be 2.28 A/mg_{Pd+Au}, greater than that of commercial palladium black.[30] Lin et al. deposited 2 nm Pd nanoparticles on carbon nanotubes and observed a peak current of 0.58 A/mg_{Pd} in 0.5 M KOH and 0.5 M EtOH.[31] Gao et al. deposited 2 nm Pd nanoparticles on polyhedrin and the resulting nanocomposites showed the onset and peak potentials at +0.387 V and +0.747 V, respectively.[32] Lei et al. prepared a nanocomposite by depositing 5 nm Pd and $NiCoO_x$ nanoparticles on carbon substrates, and the onset and peak potentials were identified at +0.443 V and +0.903 V, along with a peak current of 0.43 A/mg in the solution of 0.1 M KOH and 0.5 M EtOH.[33] Xu et al. loaded 3.6 nm Pd nanoparticles on 50 nm poly(3,4-ethyl-enedioxythiophene) particles, and the nanocomposite exhibited onset and peak potentials at +0.407 and +0.777 V.[34] Shen et al. used MgO as a support to load 10 nm Pd nanoparticles and found that the current density (85 mA/cm^2) was 3.4 times greater than that of Pd/C in 1 M KOH and 1 M EtOH. The onset and peak potentials were identified at +0.407 and +0.777 V, respectively.[35] Vizza et al. used an electrochemical milling and faceting method to deposit palladium nanoparticles (dia. 7.5 nm) on a titania nanotube array, and the resulting composite showed an onset potential of +0.21 V and peak potential of about +1 V in EOR, along with a peak current density of 201 mA/cm^2 in 2 M KOH and 10 wt% EtOH.[36]

Durability is another important parameter in the evaluation of catalyst performance. Figure 5 depicts the chronoamperometric profiles of the various catalysts when the electrode potential was stepped from +0.1 V to +0.7 V (vs. RHE). It can be seen that the current density of the Pd/hTiO_2-600 sample remained the highest at all times (up to 1200 s). For instance, even after 1000 s of continuous operation, the Pd/hTiO_2-600 still showed a current density of 0.16 mA/cm^2, which was more than twice those of Pd/C (0.06 mA/cm^2) and Pd/TiO_2 (0.07 mA/cm^2).

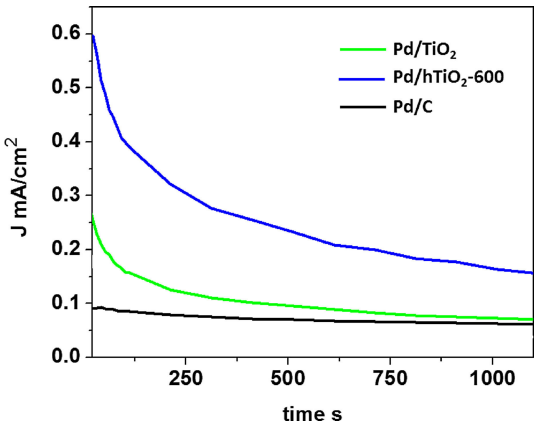

Figure 5. Chronoamperometric curves at +0.7 V with the same electrodes as in Figure 4 in 1 M KOH and 0.1 M EtOH.

The electron-transfer kinetics of ethanol oxidation at these nanocomposites was then examined by electrochemical impedance measurements. Figure 6 shows the Nyquist plots of ethanol oxidation catalyzed by the series of nanocomposites at +0.7 V. It can be seen that all samples show a semicircle, which was fitted well by the equivalent circuit depicted in the figure inset. From the fittings, the charge-transfer resistance (R_{ct}) was estimated to be 1557 Ω for Pd/TiO_2 and 1328 Ω for Pd/C, and markedly lower for the Pd/hTiO_2 series: 1081 Ω for Pd/hTiO_2-400, 813 Ω for Pd/hTiO_2-500, and only 468 Ω for Pd/hTiO_2-600. Similar trends were observed at other electrode potentials (Figure S3). This is consistent with results in the voltammetric measurements (Figure 4) where the EOR activity increased with increasing thermal annealing temperature, due to the enhanced generation of oxygen vacancies that facilitated the formation of hydroxyl species needed for the oxidation of ethanol to acetate.

Table 2. Summary of EOR performance of relevant Pd-based catalysts in recent literature.

Sample	E_{onset} [V vs. RHE]	E_a [V vs. RHE]	J_a	Particle Size [nm]
Pd/Au[30]	0.44	0.85	2.28 A/mg_{Pd+Au} (1 M KOH, 1 M EtOH)	10
Pd/CNT[31]	0.50	0.90	0.58 A/mg_{Pd} (0.5 M KOH, 0.5 M EtOH)	2
Pd/polyhedrin[32]	0.387	0.747	2 A/mg_{Pd} (1 M KOH, 0.5 M EtOH)	2
Pd/$NiCoO_x$[33]	0.443	0.903	0.43 A/mg_{Pd} (0.1 M KOH, 0.5 M EtOH)	5
Pd/PEDOT[34]	0.470	0.770	3.4 mA/cm^2 (1 M KOH, 1 M EtOH)	3.6
Pd/MgO[35]	0.407	0.777	85 mA/cm^2 (1 M KOH, 1 M EtOH)	10
Pd/TiO_2[36]	0.21	~1	201 mA/cm^2 (2 M KOH, 10wt% EtOH)	7.5
Pd/hTiO_2-600 (this work)	0.377	0.728	0.88 mA/cm^2 (1 M KOH, 0.1 M EtOH)	5

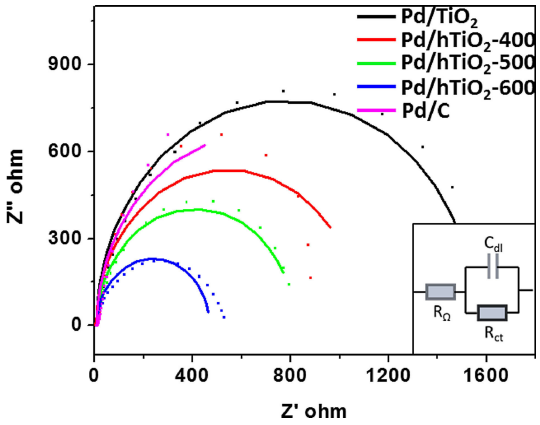

Figure 6. Nyquist plots of Pd/TiO_2, $Pd/hTiO_2$-T, and Pd/C electrodes at +0.7 V (vs. RHE). Symbols are experimental data and curves are fits by the equivalent circuit depicted in the inset, where R_Ω is the solution (uncompensated) resistance, R_{ct} is the charge-transfer resistance, and C_{dl} is the electrode double-layer capacitance.

3. Conclusion

In this study, a series of nanocomposites were prepared by depositing Pd nanoparticles onto TiO_2 nanobelts. Whereas Pd nanoparticles were rather homogeneously distributed on the as-prepared TiO_2 nanobelts, clustering of the nanoparticles was observed when the nanobelts were subjected to thermal annealing in a hydrogen atmosphere, due to partial reduction of Ti(IV) to Ti(III) and the generation of oxygen vacancies, as confirmed by XPS and EPR measurements. This was found to facilitate electrocatalytic oxidation of ethanol in an alkaline solution. In fact, the electrocatalytic activity was found to increase with increasing concentration of oxygen vacancies in the nanocomposites, which might be ascribed to the ready generation of surface-adsorbed hydroxyl groups that were needed for the oxidation of ethanol to acetate. Within the context of onset potential, anodic and cathodic peak potentials, peak current density and electron-transfer kinetics, the sample prepared with TiO_2 thermally treated at 600 °C stood out as the best catalyst among the series, with a performance markedly better than that of commercial Pd/C as well as leading results in recent literature on relevant catalysts. The results highlight the significance of structural defects of supporting substrates in the manipulation and engineering of nanoparticle electrocatalytic activity in ethanol oxidation.

Experimental Section

Materials

P25 titanium dioxide (TiO_2, Alfa Aesar), sodium hydroxide (NaOH, Fisher Scientific), hydrochloric acid (HCl, 37% v/v, Fisher Chemical), hydrogen gas (ultrahigh purity, Praxair), palladium(II) chloride ($PdCl_2$, Acros), trisodium citrate dehydrate (Fisher Scientific), sodium borohydride ($NaBH_4$, >98%, Acros), ethanol (EtOH, HPLC grade, Fisher Chemicals), carbon black Vulcan XC72 (Fuel Cell Store), and Pd/C (20 wt.%, *ca.* 4.6 nm in diameter,[37] Alfa Aesar) were used as received. Water was supplied from a Barnstead Nanopure water system (18.3 MΩ cm).

Synthesis of TiO_2 Nanobelts

TiO_2 nanobelts were synthesized by adopting a hydrothermal process reported previously.[38] Briefly, 0.1 g of commercial P25 was mixed with 20 mL of a 10 M NaOH aqueous solution, followed by hydrothermal treatment at 200 °C in Teflon-lined autoclave for 2 d. The obtained product was washed with Nanopure water for three times, affording sodium titanate nanobelts. These were then dipped in a 0.1 M HCl aqueous solution for 24 h and washed thoroughly with deionized water to produce hydrogen titanate nanobelts. TiO_2 nanobelts were obtained by annealing the hydrogen titanate in air at 600 °C for 1 h. Further annealing of the obtained TiO_2 nanobelts was carried out in a tube furnace under a hydrogen gas flow of 50 sccm at varied temperatures (400, 500 or 600 °C) for 1 h, affording hydrogen-treated TiO_2 nanobelts which were denoted as $hTiO_2$-T with T being the annealing temperature.[25]

Synthesis of Pd/TiO_2 and $Pd/hTiO_2$ Nanocomposites

In a typical synthesis of the Pd/TiO_2 nanocomposites, 5 mg of the TiO_2 nanobelts obtained above was dispersed in 10 mL of Nanopure water under sonication for 30 min to form a homogeneous suspension. Then, 525 μL of 10 mM H_2PdCl_4 and 10 mL of 0.525 mM trisodium citrate were added under magnetic stirring for 2 h. After that, 5 mL of 30 mM $NaBH_4$ was added in a dropwise fashion at the controlled temperature of 10 °C under vigorous stirring, and the solution was found to exhibit an apparent color change from orange to dark brown, signifying the formation of Pd nanoparticles. The solution was stirred for another 2 h and centrifuged at 3000 rpm for 5 min. The product was collected and washed by water and ethanol for three times and dried in a vacuum oven at room temperature overnight, affording Pd/TiO_2 nanocomposites. Palladium nanoparticles were also deposited on $hTiO_2$-T nanobelts in a similar fashion. The resulting nanocomposites were referred to as $Pd/hTiO_2$-T.

Characterization

The morphologies of the nanocomposites were characterized by transmission electron microscopy (TEM), with a Philips CM300 scope operated at 300 kV. Elemental composition and electronic structures were characterized by X-ray photoelectron spectroscopy (XPS) measurements with a PHI 5400/XPS instrument equipped with an Al K_α source operated at 350 W and 10^{-9} Torr. The crystalline characteristics were evaluated by powder X-ray diffraction (XRD) measurements with a Rigaku Mini-flex Powder Diffractometer using Cu–Kα radiation with a Ni filter (λ = 0.154059 nm at 30 kV and 15 mA). Electron paramagnetic resonance (EPR) measurements were carried out with a Bruker EMX EPR spectrometer at the X-band frequency (~9.4 GHz) using an ER 4122SHQE resonator. All EPR spectra were recorded using a power of 1 mW, a modulation amplitude of 1 G, and a modulation frequency of 100 KHz.

Electrochemistry

Electrochemical tests were carried out with a CHI 440 electrochemical workstation in a conventional three-electrode configuration, with a glassy carbon working electrode, a Ag/AgCl reference and a Pt wire counter electrode. The Ag/AgCl reference was calibrated against a reversible hydrogen electrode (RHE) and the

potentials in the present study were all reported with respect to the RHE. The glassy carbon electrode was first polished with 0.05 μm Al_2O_3 slurries to a mirror finish, and cleaned in dilute HNO_3 to remove residual Al_2O_3, followed by extensive rinsing with Nanopure water. To prepare catalyst inks, a calculated amount of the nanocomposites obtained above was suspended in ethanol at a concentration of 10 mg/mL. Then, into 1 mL of this suspension was added 4 mg of carbon black and 10 μL of Nafion under sonication for 30 min. 10 μL of the suspension was dropcast onto the polished glassy carbon electrode surface, onto which was then added 5 μL of 20% Nafion. The electrode was dried in air at room temperature before being immersed into electrolyte solutions for data acquisition. Electrochemical impedance measurements were performed with a Gamry Reference 600 electrochemical workstation within the frequency range of 100 mHz to 100 kHz and the AC amplitude of 5 mV.

Acknowledgements

This work was supported, in part, by grants from the National Science Foundation (DMR-1409396, S.W.C.) and the National Institute of Heath (GM065790, G.L.M.). TEM and XPS work was carried out at the National Center for Electron Microscopy and Molecular Foundry of the Lawrence Berkeley National Laboratory, respectively, as part of a user project.

Conflict of Interest

The authors declare no conflict of interest.

Keywords: electrooxidation · ethanol · oxygen vacancies · palladium nanoparticle · TiO_2 nanobelts

[1] E. Antolini, *J. Power Sources* **2017**, *170*, 1–12.
[2] Y. X. Bai, J. J. Wu, J. Y. Xi, J. S. Wang, W. T. Zhu, L. Q. Chen, X. P. Qiu, *Electrochem. Commun.* **2005**, *7*, 1087–1090.
[3] a) S. S. Pethaiah, J. Arunkumar, M. Ramos, A. Al-Jumaily, N. Manivannan, *Bull Mater Sci* **2016**, *39*, 273–278; b) S. Almheiri, H. T. Liu, *Int. J. Hydrogen Energy* **2015**, *40*, 10969–10978; c) T. Yamaguchi, H. Zhou, S. Nakazawa, N. Hara, *Adv. Mater.* **2007**, *19*, 592-+.
[4] C. Y. Huang, J. S. Lin, W. H. Pan, C. M. Shih, Y. L. Liu, S. J. Lue, *J. Power Sources* **2016**, *303*, 267–277.
[5] Y. Wang, S. Z. Zou, W. B. Cai, *Catalysts* **2015**, *5*, 1507–1534.
[6] W. T. Yu, M. D. Porosoff, J. G. G. Chen, *Chem. Rev.* **2012**, *112*, 5780–5817.
[7] M. S. Ahmed, D. Park, S. Jeon, *J. Power Sources* **2016**, *308*, 180–188.
[8] a) H. Idriss, *Platin. Met. Rev.* **2004**, *48*, 105–115; b) Q. G. He, W. Chen, S. Mukerjee, S. W. Chen, F. Laufek, *J. Power Sources* **2009**, *187*, 298–304; c) L. Assaud, N. Brazeau, M. K. S. Barr, M. Hanbücken, S. Ntais, E. A. Baranova, L. Santinacci, *ACS Appl. Mater. Interfaces* **2015**, *7*, 24533–24542.
[9] M. S. Ahmed, S. Jeon, *Acs Catal.* **2014**, *4*, 1830–1837.
[10] R. Z. Jiang, D. T. Tran, J. P. McClure, D. Chu, *Acs Catal.* **2014**, *4*, 2577–2586.
[11] A. L. Wang, X. J. He, X. F. Lu, H. Xu, Y. X. Tong, G. R. Li, *Angew. Chem. Int. Ed.* **2015**, *54*, 3669–3673.
[12] H. Y. Jin, T. Y. Xiong, Y. Li, X. Xu, M. M. Li, Y. Wang, *Chem. Commun.* **2014**, *50*, 12637–12640.
[13] Z. X. Yan, J. M. Xie, P. K. Shen, M. M. Zhang, Y. Zhang, M. Chen, *Electrochim. Acta* **2013**, *108*, 644–650.
[14] F. P. Hu, G. F. Cui, Z. D. Wei, P. K. Shen, *Electrochem. Commun.* **2008**, *10*, 1303–1306.
[15] M. M. O. Thotiyl, T. R. Kumar, S. Sampath, *J. Phys. Chem. C* **2010**, *114*, 17934–17941.
[16] a) Y. Ito, T. Takeuchi, T. Tsujiguchi, M. A. Abdelkareem, N. Nakagawa, *J. Power Sources* **2013**, *242*, 280–288; b) J. F. Ju, Y. J. Shi, D. H. Wu, *Powder Technol.* **2012**, *230*, 252–256; c) S. H. Kang, Y. E. Sung, W. H. Smyrl, *J. Electrochem Soc.* **2008**, *155*, B1128–B1135; d) K. Liu, Y. Song, S. W. Chen, *Nanoscale* **2015**, *7*, 1224–1232; e) S. Maheswari, P. Sridhar, S. Pitchumani, *Electrochem. Commun.* **2013**, *26*, 97–100; f) Y. H. Qin, Y. F. Li, T. Lam, Y. C. Xing, *J. Power Sources* **2015**, *284*, 186–193; g) K. I. Ozoemena, *Rsc Adv.* **2016**, *6*, 89523–89550; h) Y.-H. Qin, H.-H. Yang, R.-L. Lv, W.-G. Wang, C.-W. Wang, *Electrochim. Acta* **2013**, *106*, 372–377.
[17] W. Li, Y. Bai, F. J. Li, C. Liu, K. Y. Chan, X. Feng, X. H. Lu, *J. Mater. Chem.* **2012**, *22*, 4025–4031.
[18] a) M. H. Jang, R. Agarwal, P. Nukala, D. Choi, A. T. C. Johnson, I. W. Chen, R. Agarwal, *Nano Lett.* **2016**, *16*, 2139–2144; b) B. Santara, P. K. Giri, S. Dhara, K. Imakita, M. Fujii, *J. Phys. D Appl. Phys.* **2014**, *47*; c) M. Khan, J. Li, W. B. Cao, B. Mansoor, F. Rehman, *Int. J. Mod. Phys. B* **2014**, *28*; d) L. J. Liu, F. Gao, H. L. Zhao, Y. Li, *Appl. Catal. B-Environ* **2013**, *134*, 349–358; e) P. Liu, Y. Zhao, R. Qin, S. Mo, G. Chen, L. Gu, D. M. Chevrier, P. Zhang, Q. Guo, D. Zang, B. Wu, G. Fu, N. Zheng, *Science* **2016**, *352*, 797–800; f) E. A. Monyoncho, S. Ntais, N. Brazeau, J.-J. Wu, C.-L. Sun, E. A. Baranova, *ChemElectroChem* **2016**, *3*, 218–227.
[19] Z. Liang, T. Zhao, J. Xu, L. Zhu, *Electrochim. Acta* **2009**, *54*, 2203–2208.
[20] a) S. Bagheri, N. Muhd Julkapli, S. Bee Abd Hamid, *Scientific World J.* **2014**, *2014*; b) Y. Y. Song, C. H. Wei, X. L. Zhang, X. Wei, X. P. Song, Z. B. Sun, *Mater. Chem. Phys.* **2015**, *161*, 153–161.
[21] X. Li, Y. Zhang, T. Li, Q. Zhong, H. Li, J. Huang, *J. Power Sources* **2014**, *268*, 372–378..
[22] M. Brun, A. Berthet, J. Bertolini, *J. Electron. Spectrosc. Relat. Phenom.* **1999**, *104*, 55–60.
[23] a) X. Q. Qin, F. He, L. X. Chen, Y. H. Meng, J. Liu, N. Q. Zhao, Y. Huang, *Rsc Adv.* **2016**, *6*, 10887–10894; b) B. Palanisamy, C. M. Babu, B. Sundaravel, S. Anandan, V. Murugesan, *J. Hazard. Mater.* **2013**, *252–253*, 233–242.
[24] V. Zoulalian, S. Zurcher, S. Tosatti, M. Textor, S. Monge, J. J. Robin, *Langmuir* **2010**, *26*, 74–82.
[25] G. Wang, H. Wang, Y. Ling, Y. Tang, X. Yang, R. C. Fitzmorris, C. Wang, J. Z. Zhang, Y. Li, *Nano Lett.* **2011**, *11*, 3026–3033.
[26] S. W. Sweeney, G. Roseman, C. P. Deming, N. Wang, T. A. Nguyen, G. L. Millhauser, S. W. Chen, *Int. J. Hydrogen Energy* **2016**, *41*, 18005–18014.
[27] a) T. Su, Y. L. Yang, Y. Na, R. Q. Fan, L. Li, L. G. Wei, B. Yang, W. W. Cao, *Acs Appl. Mater. Interfaces* **2015**, *7*, 3754–3763; b) X. Pan, M. Q. Yang, X. Fu, N. Zhang, Y. J. Xu, *Nanoscale* **2013**, *5*, 3601–3614; c) M. Wajid Shah, Y. Zhu, X. Fan, J. Zhao, Y. Li, S. Asim, C. Wang, *Sci. Rep.* **2015**, *5*, 15804; d) X. Pan, Y.-J. Xu, *J. Phys. Chem. C* **2013**, *117*, 17996–18005; e) X. Y. Pan, Y. J. Xu, *Appl. Catal. A-Gen* **2013**, *459*, 34–40.
[28] S. Sarkar, R. Jana, Suchitra, U. V. Waghmare, B. Kuppan, S. Sampath, S. C. Peter, *Chem. Mater.* **2015**, *27*, 7459–7467.
[29] J. Zhang, M. Zhang, Z. Jin, J. Wang, Z. Zhang, *Appl. Surf. Sci.* **2012**, *258*, 3991–3999.
[30] H. Wang, K. Jiang, Q. L. Chen, Z. X. Xie, W. B. Cai, *Chem. Commun.* **2016**, *52*, 374–377.
[31] G. H. Yang, Y. Z. Zhou, H. B. Pan, C. Z. Zhu, S. F. Fu, C. M. Wai, D. Du, J. J. Zhu, Y. H. Lin, *Ultrason. Sonochem.* **2016**, *28*, 192–198.
[32] G. G. Pang, M. X. Sun, P. Liu, L. Hou, F. M. Gao, *Rsc Adv.* **2016**, *6*, 19734–19741.
[33] W. Wang, Y. Yang, Y. Q. Liu, Z. Zhang, W. K. Dong, Z. Q. Lei, *J. Power Sources* **2015**, *273*, 631–637.
[34] R. R. Yue, H. W. Wang, D. Bin, J. K. Xu, Y. K. Du, W. S. Lu, J. Guo, *J. Mater. Chem. A* **2015**, *3*, 1077–1088.
[35] N. Li, Y. X. Zeng, S. Chen, C. W. Xu, P. K. Shen, *Int. J. Hydrogen Energy* **2014**, *39*, 16015–16019.
[36] Y. X. Chen, A. Lavacchi, S. P. Chen, F. di Benedetto, M. Bevilacqua, C. Bianchini, P. Fornasiero, M. Innocenti, M. Marelli, W. Oberhauser, S. G. Sun, F. Vizza, *Angew Chem Int Ed* **2012**, *51*, 8500–8504.
[37] C. Y. Hu, X. Wang, *Int. J. Hydrogen Energy* **2015**, *40*, 12382–12391.
[38] P. G. Hu, G. J. Du, W. J. Zhou, J. J. Cui, J. J. Lin, H. Liu, D. Liu, J. Y. Wang, S. W. Chen, *Acs Appl. Mater. Interfaces* **2010**, *2*, 3263–3269.

Manuscript received: May 2, 2017
Accepted Article published: June 5, 2017
Version of record online: June 27, 2017